Numerical Simulation of Mechanically Adaptive Bone Remodeling around Teeth and Implants: A Comparison with Clinical Images

Kangning Su[1], Chengyao Gao[1], Guoxian Qiu[1,2], Li Yuan[3], Jie Yang[4], Jing Du[1,*]

[1] Department of Mechanical Engineering, Pennsylvania State University, University Park, PA, 16802, USA

[2] School of Intelligent Manufacturing, Changzhou Vocational Institute of Engineering, Changzhou, China

[3] Department of Stomatology Center, Shenzhen People's Hospital, 2nd Clinical Medical College of Jinan University, Shenzhen, China

[4] Division of Oral and Maxillofacial Radiology, Kornberg School of Dentistry, Temple University, Philadelphia, PA, 19122, USA

* Correspondence to: Dr. Jing Du, Department of Mechanical Engineering, 316B Leonhard Building, University Park, PA 16802

Phone: +1-814-863-1043; Fax: +1-814-865-9693; Email: jingdu@psu.edu

Other authors:

Kangning Su kxs535@psu.edu; Chengyao Gao cygao@psu.edu; Guoxian Qiu gxqiu@czie.edu.cn; Jie Yang jie.yang@temple.edu; Li Yuan yuan_li@163.com.

Abstract

In this study, the results of numerical simulation of mechanically adaptive bone remodeling were compared with clinical images. Cone beam computed tomography (CBCT) images of multiple human subjects were superimposed to obtain a continuous bone density spatial distribution map inside the mandible supporting the lateral incisor. Strain energy density in the bone under normal chewing and biting forces was computed using finite element analysis. A bone remodeling algorithm was implemented to compute the bone density distribution at equilibrium. Linear regression analysis was performed between the bone density computed by numerical simulation and that obtained from image analysis, for every trabecular bone element. The results exhibited close agreement with a coefficient of correlation of 0.8499. The bite forces were transmitted through tooth roots to the surrounding bone, thus stimulating high trabecular bone density near the roots. The bending and torsion moments on the sagittal section of the mandible resulted in lower bone density near the center than those towards the edge of the mandible. The results provide a new method to compare the results of adaptive bone remodeling simulation with experimental data and also provide model parameters to predict the bone density distribution surrounding a dental implant that replaced the tooth.

Keywords: Bone density, bone remodeling, finite element, cone beam computed tomography, dental implant

1. Introduction

Bone adapts to the change of mechanical stimulus by remodeling activities, which results in changes in bone density [1]. There have been several numerical algorithms that simulated this process. Initially, these algorithms were developed for orthopedic applications, especially for femoral heads [2,3]. Later, the algorithms were extended to dental problems, such as dental implant material selection, implant geometry design, or just mandibular bone density distribution around teeth [4–7].

In these models, when the mechanical stimulus remains in an equilibrium range, bone density remains unchanged. When the mechanical stimulus shifts outside the equilibrium range, it leads to an increase or decrease in bone density which again influences the mechanical stimulus. These cycles persist until the mechanical stimulus returns to the equilibrium range. These models are iterative, nonlinear, and multi-parameter. Our prior work on the numerical simulation of mandible bone remodeling under tooth loading has demonstrated the effects of several model parameters on the bone density distribution at the equilibrium state and also discussed the stability, uniqueness, and convergence in the models [8].

To validate these models, the computed results have been compared with optical images, radiographs, or computed tomography images. In some studies, the comparison was qualitative and was done visually [9]. Some studies compared the overall bone density or bone morphology without considering their spatial distribution [10]. Some studies compared the computed results with the grayscales in radiography or CT images in a limited number of regions of interest [11,12] A few studies compared the computed bone density with the Hounsfield unit (HU) in CT images across the whole model [13,14]. The discrepancies between the computed results and images

remained large in many of these studies. There is a need to improve the method that compares the computed results with images quantitatively and thoroughly.

In this study, a new method is proposed to compare the bone remodeling simulation results with the clinical images. Cone beam computed tomography (CBCT) images of the mandibles for multiple human subjects are superimposed to obtain the average outline of the mandible and the average bone density distribution around the lateral incisor. Finite element models are built based on the average outline from CBCT images. A bone remodeling algorithm is carried out to compute the bone density distribution around the tooth under normal biting and chewing forces. The computed bone density for every element was compared with the bone density obtained from CBCT images at the corresponding location. Applied loads, boundary conditions, and algorithm parameters are adjusted to achieve the best linear fit. The same loads, boundary conditions, and algorithm parameters are used to predict the bone density surrounding a dental implant that replaces the tooth. The implications of the results and the limitations of the current method are discussed.

2. Materials and Methods

2.1 Calibration of CBCT scanner

A CBCT scanner (VGi, NewTom, Verona, Italy) in a dental clinic was calibrated using two self-costumed phantoms. One phantom was an acrylic plate with 38 mm thickness and 148 mm diameter that was comparable to the diameter of a human head. The other phantom (Fig. 1a) was the same size acrylic plate that contained 4 holes with 25 mm diameter that were filled with aluminum, polyvinyl chloride (PVC), water, and air, respectively. The phantoms were then

scanned in the CBCT scanner using 1 mA scanning current and 110 keV voltage. The isometric voxel size of the images was 0.15 mm.

The X-ray mass attenuation coefficients, μ/ρ, for each phantom material at various energy levels from 10 to 150 keV were obtained from the National Institute of Standards and Technology (NIST) database [15]. The X-ray linear attenuation coefficients, μ, were obtained by multiplying μ/ρ with their densities, ρ, respectively [15,16]. Simple linear regression analysis was performed between the average grayscale values in the CBCT images and the linear attenuation coefficients for the five phantom materials at various energy levels, respectively. The energy level that resulted in the highest coefficient of determination was defined as the effective energy level [17].

The Hounsfield unit of each material is given by

$$HU = 1000 \times \frac{\mu - \mu_{water}}{\mu_{water} - \mu_{air}} \quad (1)$$

where μ is the linear attenuation coefficient of each specific material at the effective energy level; μ_{water} and μ_{air} are the linear attenuation coefficients of water and air, respectively [17].

2.2 Analysis of CBCT images

This study received an exemption from the institutional review board (IRB) at Penn State University (STUDY00006032). CBCT images of 33 human subjects were obtained from the same dental clinic. These images were previously collected for various dental treatment purposes before this study. The subjects were randomly selected and included 12 females and 21 males ranging from 23 to 76 years old. The scanning parameters were the same as those used for the phantoms in section 2.1.

The sagittal cross-sectional images at the center of lateral incisors were extracted from each CBCT image stack using Avizo software (Thermo Fisher Scientific, Waltham, Massachusetts, US). The incisors that were lost, had root canal treatment, or had severe bone recess were excluded, thus 42 cross-sectional images were obtained. A few representative images were presented in Fig. 2. Using Avizo software, the background (air) and the surrounding soft tissues were cropped out. Each remaining image was divided into 4 parts, tooth, lingual and buccal halves of the alveolar bone holding the tooth, and the base of the mandible (Fig. 2). The cusp of the tooth, the apex of the tooth root, the lingual and buccal bone crest, and the lowest point of the mandible were identified in the images (Fig. 2).

The average outline was calculated using the following steps. The average height of each part was calculated among all cross-sectional images, respectively, and each part was rescaled to its average height. Inside each part, row by row, the mean coordinates of the leftmost and rightmost pixels were calculated to obtain the left and right outlines, respectively. The average outlines of the 4 parts were then pieced together to form an average outline for the lateral incisor and bone in the mandible.

The average bone density distribution was then calculated. Each cross-sectional image was mapped to the average outline by mapping the grayscale values in the rescaled parts row by row to the average outline. For each pixel point location, the average grayscale value among all cross-sectional images was calculated. They were then converted to X-ray linear attenuation coefficient, μ, using the linear relationship obtained in the CBCT calibration process (section 2.1). The X-ray linear attenuation coefficient was converted the HU scale using equation (1), and lastly converted to apparent bone density, which is given by

$$\rho = \frac{\rho_{cortical} \cdot HU}{HU_{cortical}} \quad (2)$$

where ρ is the apparent bone density and $\rho_{cortical}$ is the apparent bone density for cortical bone, which was assumed to be 2.0 g/cm^3 [18], HU is the Hounsfield unit for this pixel location and $HU_{cortical}$ is the averaged Hounsfield unit for the cortical bone, which was obtained from 30 randomly-selected areas of interest in cortical bone in the cross-sectional images for incisors.

2.3 Bone remodeling around a tooth

Finite element analysis was carried out to calculate the strain energy density in the mandible surrounding a lateral incisor under normal chewing and biting forces using the Abaqus 2021 software package (Dassault Systemes Simulia Corporation, Providence, RI). A model was built based on the average outline of the tooth-bone structure obtained from the CBCT images analysis in section 2.2 (Fig. 3a). The model contained 6,569 4-node linear quadrilateral elements, with 1,555 of them representing the trabecular bone. The model consisted of dentin, pulp, periodontal ligament (PDL), cortical bone, and trabecular bone. The interfaces of PDL-dentin and PDL-bone were fully bonded.

All materials were assumed to be linear elastic and isotropic. The non-linear viscoelastic behaviors of PDL were neglected because its mechanical behaviors under normal mastication loading conditions fall in the linear elastic region of the constitutive model [19] and do not significantly affect the strain and stress in the bone. The material properties used in the simulation are listed in Table 1 [20].

The initial apparent density for all trabecular bone elements was assumed to be 0.8 g/cm^3. The nominal modulus for trabecular bone was given by Carter and Hayes [21] and has then adapted to be:

$$E = C\rho^3 \quad (3)$$

where E is the nominal modulus in MPa, C is a constant of 3790 MPa·cm^9/g^3 and ρ is the apparent density in g/cm^3 [19,22–24].

As illustrated in Fig. 3a, a load was applied on the cusp of the incisor to mimic the normal chewing and biting forces. Part of the base of the mandible was fully constrained. A torsion moment was applied near the center of the trabecular bone region. Uniform pressures were applied over several regions at the border of the mandible (Fig. 3a) [4]. The total elastic strain energy density in the incisor-bone structure was calculated.

The strain energy density per unit bone mass, U/ρ, was chosen to be the mechanical stimulus, S, in the bone remodeling algorithm. The change of apparent bone density in each iteration was given by

$$\Delta\rho = \begin{cases} -0.05\rho, & bone\ loss\ at\ constant\ rate, & for\ S < S_l \\ (S-(1-\delta)S_0)B\Delta t, & bone\ loss, & for\ S_l < S < (1-\delta)S_0 \\ 0, & equilibrium, & for\ (1-\delta)S_0 < S < (1+\delta)S_0 \\ (S-(1+\delta)S_0)B\Delta t, & bone\ growth, & for\ (1+\delta)S_0 < S < S_u \\ 0.05\rho, & bone\ growth\ at\ constant\ rate, & for\ S > S_u \end{cases} \quad (4)$$

where S_0 is the reference value for the mechanical stimulus. S_l and S_u are the lower and upper limits of the mechanical stimulus; δ is the half-width of the equilibrium zone; B is the remodeling rate constant, and Δt is the time step. Also, the trabecular bone density was mandated to be higher than 0.1 g/cm^3 to prevent negative density and lower than 2.0 g/cm^3, the apparent density of cortical bone [25].

The bone remodeling algorithm was implemented by the self-customized Python scripts via the Abaqus scripting interface that iterated the above-mentioned finite element analysis, which calculated the total elastic strain energy density in the incisor-bone structure (refer to online

supplementary material). The computer server included 20 CPU processors (10-core Intel Xeon E5-2680 2.8 GHz), 256 GB random access memory (RAM), and a 40-core GPU processor (NVIDIA GK106GL Quadro K4000) for acceleration in Abaqus. In each iteration, the apparent density of trabecular bone was updated using the forward Euler method in equation (4), with $B\Delta t$ of 1.5 $g^2/(J \cdot cm^3)$, and δ of 15%. The lower and upper limit of $\Delta\rho$ was directly mandated for each element in the Python scripts, without calculating the lower and upper limit of the mechanical stimulus. Then the elastic modulus for each trabecular bone element was updated using equation (3). The process was repeated until the average bone density in all trabecular bone elements changed by less than 0.02% in the last two iteration steps. A flow chart of the implementation of the bone remodeling algorithm is presented in Fig. 4.

The bone density of every trabecular bone element was compared with the bone density obtained from CBCT image analysis. In total, 1,555 elements were compared. First, the bone density of each element was extracted. Next, corresponding to the location of the centroid of each element, the bone density values were extracted from CBCT image analysis results. Then, simple linear regression analysis was performed between the bone density values obtained from numerical simulation and those obtained from CBCT images for each element. Simple linear regression analysis was commonly used in the literature to compare the computational results with clinical or experimental images [11,12,14]. Ideally, the slope should be 1 and intercept should be 0. The applied loads and the reference value of the mechanical stimulus were adjusted to achieve the best linear fit.

2.4 Bone remodeling around a dental implant

Finite element analysis was then carried out to calculate the strain energy density in the mandible surrounding a dental implant under normal chewing and biting forces. A model was built

based on the average outline obtained from the CBCT images analysis in section 2.2, with the tooth replaced by a titanium alloy dental implant with an abutment and a zirconia crown. The gap in the alveolar socket was filled with woven bone (Fig. 3b). The model contained 8,109 4-node linear quadrilateral elements, with 1,077 of them representing the woven bone and 1,754 of them representing the trabecular bone. The model consisted of a crown, an implant with an abutment, woven bone, cortical bone, and trabecular bone. The interface between implant and bone was fully bonded.

All materials were assumed to be linear elastic and isotropic. The material properties used in the simulation are listed in Table 1 [26–28]. The PDL is heterogeneous and anisotropic. It was simplified as an isotropic linear elastic material in the finite element models. The elastic modulus of PDL has a wide range in the literature. The value that was chosen in this study, 70.1 MPa, was often used in other finite element simulations [19,29,30]. Using equation (3), the initial apparent density for woven bone was determined to be 0.79 g/cm^3. The initial apparent density for trabecular bone was assigned based on the results from the bone remodeling simulation around the tooth in Section 2.3. As illustrated in Fig. 3b, the same boundary conditions and applied loads determined from the comparison of tooth-bone simulation and CBCT image analysis (Section 2.3) were applied in the implant-bone model.

The total elastic strain energy density in the implant-bone structure was calculated. The bone remodeling algorithm in equation (4) was implemented. In each iteration, the apparent density of woven bone and trabecular bone was updated using the forward Euler method with $B\Delta t$ of 0.1 $\mathrm{g}^2/(\mathrm{J}\cdot\mathrm{cm}^3)$ and other parameters unchanged. The process was repeated until the average bone density in all woven bone and trabecular bone elements changed by less than 0.002% in the last two iteration steps.

3. Results

3.1 Bone density distribution around a tooth determined from CBCT images

The coefficients of determination for the simple linear regression between the X-ray linear attenuation coefficients and the grayscale in CBCT images for the five phantom materials were obtained at various energy levels from 10 to 150 keV (Fig. 4a). The highest coefficient of determination was 0.9928 at the energy level of 76 keV, which was therefore determined as the effective energy level. The X-ray linear attenuation coefficients, μ, for each phantom material at the effective energy level are listed in Table 2. The relationship between linear attenuation coefficient and grayscale in CBCT images was obtained, which gives

$$\mu = 0.0002432GV + 0.1947 \quad (5)$$

where GV is the CBCT image grayscale (Fig. 4b). The Hounsfield unit (HU) of each phantom material was calculated using equations (1) and (5) and listed in Table 2.

The average outline of the mandible bone supporting the lateral incisor is presented in Fig. 5a together with the dashed line showing the standard deviation. The top of the outline shows an alveolar socket that surrounds the tooth root. The crest of the alveolar bone was missing because the quality of CBCT images was not high enough to clearly show it for every patient. Prominence can be seen on the external surface of the base of the mandible, which is the mental protuberance that forms the chin. Figure 5b shows the averaged grayscale images at the center of lateral incisors in the sagittal plane. The averaged HU for cortical bone was calculated to be 1007.87±122.75.

The average bone density distribution map is presented in Fig. 5c. The bone density of cortical bone was ~ 2.0 g/cm^3 on the buccal side and ~1.9 g/cm^3 on the lingual side of the mandible. Generally, the trabecular bone density was between 0.5 and 1.6 g/cm^3. It is relatively high

surrounding the tooth root (~1.2 g/cm^3), also high near the base of the mandible (~1.2 g/cm^3), but relatively low around the center of the mandible, especially towards the lingual side (~0.5 g/cm^3). The standard deviation of bone density (Fig. 5d) is the smallest in the cortical bone at the lingual side (~ 0.1 g/cm^3), and the largest at the boundary between cortical and trabecular bone (~ 0.6 g/cm^3).

In the bone density distribution along a horizontal line near the center of the mandible (Figs. 4e), it can also be seen that the bone density was close to 2.0 g/cm^3 in the cortical bone. The trabecular bone density reduced from ~0.65 g/cm^3 on the buccal side to ~0.5 g/cm^3 on the lingual side.

3.2 Computed bone density distribution around a tooth

The reference value for the mechanical stimulus, S_0, was determined to be 0.012 J/g. The applied loads were determined to be a concentrated load of 64.03 N on the cusp of the incisor, a torsion moment of 300 N·mm near the center of the trabecular bone region, and uniform pressures of 3, 10, and 15 MPa over several regions at the border of the cortical bone (Fig. 3a), respectively.

In the numerical simulation, the average bone density of all trabecular bone elements (Fig. 6) increased rapidly in the first few iterations; then the bone density change rate reduced. The iterations stopped after the 36th iteration when the average bone density of all trabecular bone elements was 0.878 g/cm^3. The distribution of bone density also gradually changed over the iteration steps (Fig. 7). It gradually increased near the tooth root and the base of the mandible. After the 36th iteration, bone density was ~1.5 g/cm^3 near the tooth root and ~ 1.2 g/cm^3 near the base of the mandible. Bone density also decreased at the center of the mandible. Especially at the lingual side of the mandible, it was ~ 0.5 g/cm^3 after the 36th iteration (Fig. 7).

The bone density distribution obtained from bone remodeling simulation (Fig. 7) was compared with those from CBCT image analysis (Fig. 5c). Simple linear regression between the bone density at all element locations resulted in a coefficient of determination, R^2, of 0.7223 (Fig. 8), i.e. a coefficient of correlation, R, of 0.8499. The slope and intercept of the linear fit were 1.0276 and 0.0888, respectively.

3.3 Computed bone density distribution around a dental implant

The average bone density of all woven bone and trabecular bone elements increased rapidly in the first few iterations. Then the bone density change rate reduced (Fig. 9). The iterations stopped after the 59^{th} iteration when the average bone density of all trabecular bone and woven bone elements was 0.855 g/cm^3. The bone density near the implant shoulder increased from an initial value of 0.79 g/cm^3 for the woven bone to about 1.8-2.0 g/cm^3 (Fig. 10). The bone density distribution in the trabecular bone region did not change significantly.

4. Discussion

4.1 Comparison of simulation results and experimental data

The validity of numerical simulations of bone mechanics and adaptive bone remodeling is often questioned due to the complex mechanical properties of bone and complex loads and boundary conditions in mandibles. To validate the mechanically adaptive bone remodeling simulations, several prior studies have attempted to compare the computed results with experimental data.

In an earlier work by Weinans et al., the overall bone area fraction on transverse sections of the femur was compared between simulation and radiograph in animal experiments [10], but the spatial distribution of bone density was not discussed. In the work of Chou et al., the quality of CT

images was too low to show trabecular bone and to compare with simulation results [9]. In the work of Reina et al., the CT images show discrete single trabeculae, but they were difficult to be quantitatively compared with the continuous bone density distribution from their simulations [7]. Thus, they compared the computed elastic modulus with those from experimental measurements at one spot in the cortical bone [7]. However, these experiments couldn't be performed *in vivo*, thus its potential for clinical applications was limited. Some other bone remodeling algorithms can simulate adaptive trabecular microstructures. When comparing with experimental results, the comparison was limited to the bone morphology index for the whole model, such as bone volume fraction, and trabecular thickness [31–33].

Pérez et al. compared the bone density distribution by calculating the differences between the bone density computed by their simulation and that converted from CT images across the whole model [13]. In a large portion of the trabecular bone region, the relative difference was greater than 44% [13]. Li et al. performed a linear regression between the computational results and clinical CT images in several regions of interest (ROIs) in mandibles and maxillae and obtained R^2 up to 0.65 [11,12]. Sharma et al. compared the bone density from their simulation and CT images at all element and node locations across the glenoid models and obtained R^2 up to 0.48 [14].

In this study, the analysis of CBCT images of a group of subjects provided a new method for the comparison of computed results and experimental data. The difficulty in previously existing validation methods was associated with the low image quality or discrete pattern of trabeculae. In this study, by superimposing high quality CBCT images for multiple subjects, the different discontinuous trabecular structures in each individual were converted to a continuous bone density spatial distribution map (Fig. 5c). Although mandibles exhibit large individual variations in terms

of size, shape, bone volume fraction, and trabecular microstructures (Fig. 2), the common features in the anatomy of the mandible and common trend in bone density distribution were obtained. It also enabled improved quantitative comparison with numerical simulation results. Instead of comparing limited number of ROIs, the simulation results and the CBCT image analysis results were compared for every trabecular bone element inside the model. The spatial distribution of bone density computed from bone remodeling simulation was in good agreement with that obtained from CBCT image analysis (Fig. 8). The R^2 of 0.7223 was higher than that in previous works [11,12,14]. The slope of 1.0276 was close to 1. The intercept of 0.0888 was close to 0. The improved results can be attributed to the new image analysis method and comparison method proposed in this study.

CBCT is widely used in dental clinics because of its low radiation dose, rapid scanning time, and affordable cost [34]. CBCT images have been used to estimate bone density [17,22,35], and its correlation with Lekholm and Zarb ratings of bone quality [36], the primary stability of the implants [37], and bone fracture [38]. However, there are still concerns about the accuracies in the bone density calculated based on the grayscales in CBCT, due to the artifacts in CBCT images [22,39]. In this study, the HU variation was calculated based on a full range from -1000. It decreased from 20.35% to 11.90% with increasing HU values from 0 to 1541.2 for five phantom materials. Since the HU values of trabecular bone ranged from 252 to 907, the uncertainties in the HU values and the bone density for trabecular bone were estimated to be about 12.5% using linear interpolation.

4.2 Bone density distribution and boundary conditions

The average bone density distribution obtained in this study (Fig. 5c) represents the common trends of bone density distribution among multiple human subjects. It adds new information to the

current knowledge of the spatial distribution of mandible bone density. The spatial distribution of trabecular bone density and its relationship to mechanical stimulation are important, as they are related to periodontal diseases [23], the stability and success of dental implants [40], and even osteoporosis [41]. In the future, the current image analysis method can potentially be extended to study the trabecular bone density distribution for different groups of subjects, for example, subjects with and without periodontal diseases.

Moreover, the relationship between bone density distribution and mechanical stimulations was revealed through the bone remodeling simulation in this study. The bite forces applied to teeth were transmitted through the tooth roots to the bone surrounding them, thus stimulating high trabecular bone density near the tooth roots (Figs. 5c and 7). The torsion moments on the sagittal section of the mandible resulted in lower strain energy density near the center of the section than that towards the periphery of the section. Therefore, the trabecular bone density near the center of the section was also lower than that towards the periphery of the section (Figs. 5c and 7). It was especially low towards the lingual side, due to the combined effect of torsion and pressure that were applied in the models. The distributed pressures at the edge of the models further affected the bone density at the edge of the mandible.

The loads and boundary conditions applied in the numerical models in this study are the equivalent loading conditions that can represent the mechanical stimulations in physiological loading. The forces applied on a mandible include bite forces on teeth during mastication and swallowing, forces deployed by masticatory muscles, and reaction forces on the temporomandibular joints (TMJ). In the literature, maximum bite force in the incisor region was measured to be from 111 to 244 N. It was distributed on several incisors and varied for subjects of different ages, genders, and races [42,43]. Considering the bite force that may distribute on a single

incisor, a load of 64.03 N that was applied in the finite element model in this study was within the reasonable range of normal chewing and biting force. There are nine pairs of masticatory muscles applying forces of different magnitudes and in different directions. There were studies using computer modeling to estimate the forces generated by individual muscle groups [44,45], but accurate experimental measurements have not been done to the best of our knowledge.

The combination of bite force, muscle forces, and joint forces resulted in sagittal bending [46], torsion, lateral transverse bending, and shear on the 2D sagittal plane. In the bone remodeling algorithm (equation 4), strain energy density per unit bone mass was chosen to be the mechanical stimulus. Torsion and bending both result in low strain energy density at the center of the structure. Distributed pressure and shear force resulted in relatively uniform strain energy density throughout the plane. Therefore, in the models in the current study (Fig. 3), a torsion moment was applied near the center of the trabecular bone region to mimic the bending moment and torsion, while distributed pressure was applied at the border of the cortical bone to mimic the shear force. The application of distributed pressure can also be found in prior works by Chou et al. [4]. The values of the applied loads in this study were adjusted to achieve the best linear fit between the bone density calculated from bone remodeling simulation and CBCT image analysis. Hence the boundary conditions and applied loads used in this study represent the equivalent mechanical stimulation to maintain the bone density distribution around the tooth. After the tooth was replaced by an implant, assuming that the same loads and boundary conditions will be applied to the implant-bone structure, finite element simulation and bone remodeling algorithms were carried out to predict the bone density around the implant.

4.3 Limitations

A major limitation of the current study is that the image analysis in the current work was limited to 2-dimensional (2D) sections. Since the finite element model was built based on the image analysis results, it was also limited to 2D. A direction of future work would be to extend the current methods to three-dimensional (3D) image stacks and 3D models. The loads and boundary conditions can also be better defined and more realistic if the finite element model can be extended to 3D in the future. Another limitation of the current study is the lack of experimental evidence for many simulation parameters used in this study. This could possibly be a direction for future works.

A weakness of the bone remodeling algorithm used in this study is that it did not consider bone resorption due to overloading. The large bone density near the implant shoulder indicates large mechanical stimulation in the area. If bone resorption due to overloading is considered, instead of bone apposition, the bone loss could occur in this region [47]. Moreover, stress shielding phenomena was not observed in the results. This may be another limitation of the current study. A possible direction in the future would be to compare the simulation results with CBCT images collected before and after implant placement. Another limitation is that the current results represent the general trends for multiple individuals. In the future, further work is needed to extend the current method to individual-specific models and comparisons with individual data.

The forward Euler method used in this study is not very accurate and becomes unstable for large time steps. According to the results in our previous parametric study [8], a few approaches was taken in current study to enhance stability and convergence. The product of remodeling rate and time step, $B\Delta t$, was set to small; An equilibrium zone was set near the reference value of the mechanical stimulus; The density change rate had lower and upper limits; Also, the algorithm was stopped when the change of bone density slowed down (Figs. 7 and 10) because in our previous parametric study [8] and other group's work [48,49], it was discovered that excessive iteration

steps may lead to instability and checkerboard phenomenon. Nevertheless, future work should seek alternative approaches to carry out the bone remodeling algorithm.

5. Conclusions

In this study, the results of numerical simulation of mechanically adaptive bone remodeling were compared with clinical images. CBCT images of multiple human subjects were analyzed to obtain the average outline of the mandible and spatial distribution of bone density in the mandible surrounding a lateral incisor. The bone density distribution around the tooth computed by bone remodeling algorithms was in good agreement with that obtained from CBCT images. The relationship between the bone density distribution and the mechanical stimulations on the tooth-bone construct was also explained. The results added new information to the current knowledge of the spatial distribution of bone density in the mandible, and also provided a new method to compare the results of numerical simulation of mechanically adaptive bone remodeling with experimental data. The results also provided model parameters to predict the bone density surrounding a dental implant that replaced the tooth, including boundary conditions and applied loads in the finite element models and the parameters for the bone remodeling algorithm.

Conflict of Interest Statement

We acknowledge that all authors do not have any conflict of interest, and were fully involved in the study and preparation of the manuscript.

Acknowledgment

This research was partially supported by the National Science Foundation under Grant Numbers DMR-2144614. The authors are grateful to the program manager, Dr. Nitsa Rosenzweig, for her encouragement and support. The authors would like to thank the Institute for Computational

and Data Science (ICDS) at Penn State University for providing software, computing cores, and storage.

References

1. J. Wolff, *The Law of Bone Remodelling* (Springer Berlin Heidelberg, Berlin, Heidelberg, 1986).

2. G. S. Beaupré, T. E. Orr, and D. R. Carter, J. Orthop. Res. **8**, 662 (1990).

3. R. Huiskes, H. Weinans, H. J. Grootenboer, M. Dalstra, B. Fudala, and T. J. Slooff, J. Biomech. **20**, 1135 (1987).

4. H.-Y. Chou, J. J. Jagodnik, and S. Müftü, J. Biomech. **41**, 1365 (2008).

5. J. Li, H. Li, L. Shi, A. S. L. Fok, C. Ucer, H. Devlin, K. Horner, and N. Silikas, Dent. Mater. **23**, 1073 (2007).

6. D. Lin, Q. Li, W. Li, S. Zhou, and M. V. Swain, Compos. Part B Eng. **40**, 668 (2009).

7. J. M. Reina, J. M. García-Aznar, J. Domínguez, and M. Doblaré, J. Biomech. **40**, 828 (2007).

8. K. Su, L. Yuan, J. Yang, and J. Du, Sci. Rep. **9**, 14887 (2019).

9. H. Y. Chou, D. Satpute, A. Müftü, S. Mukundan, and S. Müftü, Comput. Methods Biomech. Biomed. Engin. **18**, 269 (2015).

10. H. Weinans, R. Huiskes, B. Van Rietbergen, D. R. Sumner, T. M. Turner, and J. O. Galante, J. Orthop. Res. **11**, 500 (1993).

11. Z. Liao, N. Yoda, J. Chen, K. Zheng, K. Sasaki, M. V. Swain, and Q. Li, Biomech. Model. Mechanobiol. **16**, 411 (2017).

12. K. Zheng, N. Yoda, J. Chen, Z. Liao, J. Zhong, S. Koyama, C. Peck, M. Swain, K. Sasaki, and Q. Li, Biomech. Model. Mechanobiol. **19**, 133 (2020).

13. M. A. Pérez, P. Fornells, M. Doblaré, and J. M. García-Aznar, Comput. Methods Biomech. Biomed. Engin. **13**, 71 (2010).

14. G. B. Sharma, R. E. Debski, P. J. McMahon, and D. D. Robertson, J. Biomech. **42**, 1460 (2009).

15. J. H. Hubbell and S. M. Seltzer, Http://Physics.Nist.Gov/Xaamdi (2004).

16. Interstate Plastics, (2018).

17. P. Mah, T. E. Reeves, and W. D. McDavid, Dentomaxillofac. Radiol. **39**, 323 (2010).

18. J. K. Gong, J. S. Arnold, and S. H. Cohn, Anat. Rec. **149**, 325 (1964).

19. C. Field, Q. Li, W. Li, M. Thompson, and M. Swain, J. Biomech. **43**, 1771 (2010).

20. M. Su, H. Chang, Y. Chiang, J. Cheng, L.-J. Fuh, C.-Y. Wang, and C.-P. Lin, J. Dent. Sci. **8**, 121 (2013).

21. D. R. Carter and W. C. Hayes, J. Bone Joint Surg. Am. **59**, 954 (1977).

22. R. Molteni, Oral Surg. Oral Med. Oral Pathol. Oral Radiol. **116**, 105 (2013).

23. M. Tezal, J. Wactawski-Wende, S. G. Grossi, A. W. Ho, R. Dunford, and R. J. Genco, J.

Periodontol. **71**, 1492 (2000).

24. H. Weinans, R. I. K. Huiskes, H. Weinans, and B. van Rietbergen, Clin. Orthop. Relat. Res. 124 (1992).

25. M. Sogo, K. Ikebe, T.-C. Yang, M. Wada, and Y. Maeda, Clin. Implant Dent. Relat. Res. **14**, e183 (2012).

26. Q. Mao, K. Su, Y. Zhou, M. Hossaini-Zadeh, G. S. Lewis, and J. Du, J. Mech. Behav. Biomed. Mater. **94**, 229 (2019).

27. J. Du, X. Niu, N. Rahbar, and W. Soboyejo, Acta Biomater. **9**, 5273 (2013).

28. J. García-Rodríguez and J. Martínez-Reina, Biomech. Model. Mechanobiol. **16**, 159 (2017).

29. I. A. V. P. Poiate, A. B. de Vasconcellos, R. B. de Santana, and E. Poiate, J. Periodontol. **80**, 1859 (2009).

30. A. M. Weinstein, J. J. Klawitter, and S. D. Cook, J. Biomed. Mater. Res. **14**, 23 (1980).

31. T. G. Morgan, M. P. G. Bostrom, and M. C. H. van der Meulen, J. Biomech. **48**, 875 (2015).

32. K. ichi Tsubota, Y. Suzuki, T. Yamada, M. Hojo, A. Makinouchi, and T. Adachi, J. Biomech. **42**, 1088 (2009).

33. C. Boyle and I. Y. Kim, J. Biomech. **44**, 935 (2011).

34. W. C. Scarfe and A. G. Farman, Dent. Clin. North Am. **52**, 707 (2008).

35. K. Andruch and A. Płachta, Adv. Clin. Exp. Med. **24**, 1071 (2015).

36. P. Aranyarachkul, J. Caruso, B. Gantes, E. Schulz, M. Riggs, I. Dus, J. M. Yamada, and M. Crigger, Int. J. Oral Maxillofac. Implants **20**, 416 (2005).

37. K. Isoda, M. Sogo, K. Koyano, Y. Ayukawa, Y. Tsukiyama, M. Sogo, Y. Matsushita, and K. Koyano, Clin. Oral Implants Res. **23**, 832 (2012).

38. J.-T. Hsu, Y.-J. Chen, M.-T. Tsai, H. H.-C. Lan, F.-C. Cheng, M. Y. C. Chen, and S.-P. Wang, PLoS One **7**, e50008 (2012).

39. R. Pauwels, R. Jacobs, S. R. Singer, and M. Mupparapu, Dentomaxillofac. Radiol. **44**, 20140238 (2015).

40. I. Turkyilmaz and E. A. McGlumphy, BMC Oral Health **8**, 32 (2008).

41. K. Horner, H. Devlin, C. W. Alsop, I. M. Hodgkinson, and J. E. Adams, Br. J. Radiol. **69**, 1019 (1996).

42. S. C. H. Regalo, C. M. Santos, M. Vitti, C. A. Regalo, P. B. de Vasconcelos, W. Mestriner, M. Semprini, F. J. Dias, J. E. C. Hallak, and S. Siéssere, Arch. Oral Biol. **53**, 282 (2008).

43. S. Kiliaridis, H. Kjellberg, B. Wenneberg, and C. Engström, Acta Odontol. Scand. **51**, 323 (1993).

44. G. J. Nelson, Three Dimensional Computer Modeling of Human Mandibular Biomechanics,

1986.

45. O. Röhrle and A. J. Pullan, J. Biomech. **40**, 3363 (2007).

46. B. Sarrafpour, C. Rungsiyakull, M. Swain, Q. Li, and H. Zoellner, Arch. Oral Biol. **57**, 1070 (2012).

47. T.-J. Oh, J. Yoon, C. E. Misch, and H.-L. Wang, J. Periodontol. **73**, 322 (2002).

48. N. Garijo, J. R. Fernández, M. A. Pérez, and J. M. García-Aznar, Comput. Methods Appl. Mech. Eng. **271**, 253 (2014).

49. J. Martínez-Reina, J. Ojeda, and J. Mayo, PLoS One **11**, e0148603 (2016).

Tables

Table 1 Material properties used in the finite element simulations

Materials	Young's Modulus (MPa)	Poisson's ratio
Dentin	18600	0.3
Pulp	2	0.45
PDL	70.1	0.45
Cortical Bone	15,000	0.3
Titanium alloy	110,000	0.31
Zirconia	205,000	0.3
Woven Bone	1,900	0.34

Table 2 Grayscale, material properties and results in the calibration of CBCT scanner

Materials	Air	Water	PMMA	PVC	Aluminum
Grayscale	-898.4±77.9	-7.5±159.0	-145.1±163.36	99.7±185.9	1648.5±236.3
X-ray mass attenuation coefficient, μ/ρ (cm^2/g) [15]	0.173	0.132	0.160	0.391	0.224
Density, ρ (g/cm^3) [15]	0.0012	1.00	1.19	0.55 [16]	2.70
X-ray linear attenuation coefficient, μ (cm^{-1})	0.000208	0.132	0.190	0.215	0.606
Hounsfield unit (HU)	-1000±99.7	0±203.5	121.5±209.1	139.5±145.2	1541.2±302.5
Variation in HU	N/A	20.35%	18.64%	12.74%	11.90%

List of Figures

Fig. 1. (a) A photo and (b) a slice of CBCT image for one of the phantoms that were used in the calibration of CBCT scanner. 1 – aluminum; 2 - PVC foam; 3 – air; 4 – water; and 5 – acrylic.

Fig. 2. Representative sagittal sections of CBCT image for lateral incisors in mandible. White arrow – buccal plate; Black arrow - mental spine.

Fig. 3. Finite element model of (a) a lateral incisor and (b) an implant, respectively, in mandible including applied loads and boundary conditions.

Fig. 4. Flow chart of the bone remodeling simulation

Fig. 5. (a) Coefficient of determination obtained from simple linear regressions between X-ray linear attenuation coefficient and CBCT images grayscales for 5 materials at various energy levels; (b) Linear regression line at the effective energy level of 76 KeV.

Fig. 6. Results obtained from analysis of CBCT images of mandible around lateral incisors: (a) Average outline of mandible; (b) Averaged image intensity; (c) Average bone density distribution; (d) The standard deviation of bone density and (e) Bone density distribution along the line in (b) and (c).

Fig. 7. Adaptation of average bone density in all trabecular bone elements around a tooth in the bone remodeling simulation.

Fig. 8. Adaptation of bone density distribution around a tooth at the 0^{th}, 6^{th}, 18^{th}, and 36^{th} iteration in the bone remodeling simulation.

Fig. 9. Quantitative comparison of bone density computed by bone remolding numerical simulation and obtained from CBCT image analysis.

Fig. 10. Adaptation of average bone density in all woven bone and trabecular bone elements around an implant in the bone remodeling simulation.

Fig. 11. Adaptation of bone density distribution around an implant at the 0^{th}, 10^{th}, 30^{th}, and 59^{th} iteration in the bone remodeling simulation.

(a)

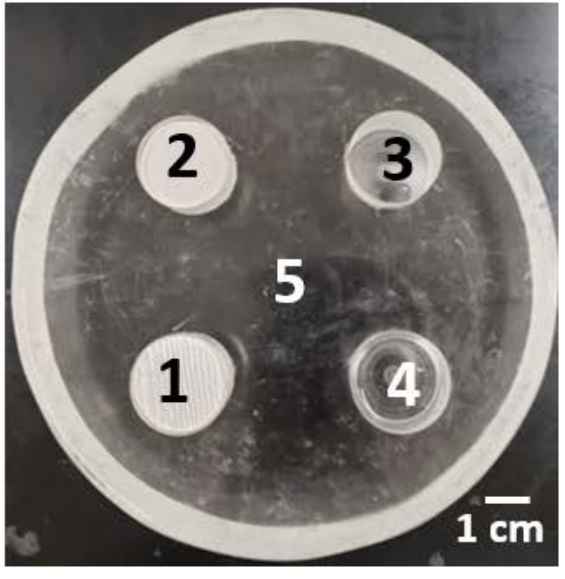

(b)

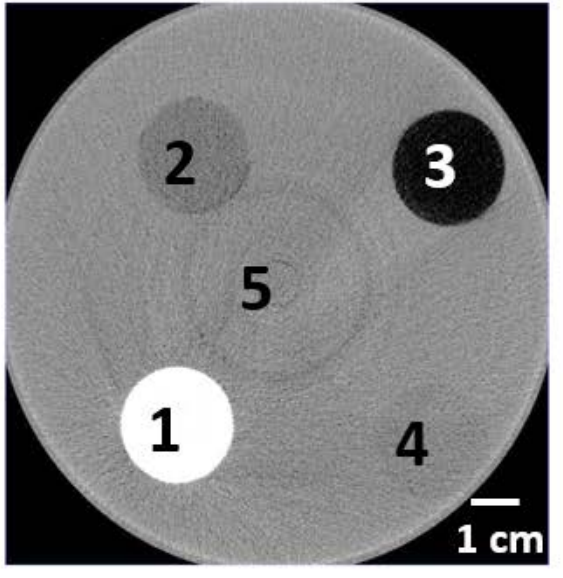

1 - Aluminum
2 - PVC foam
3 - Air
4 - Water
5 - Acrylic

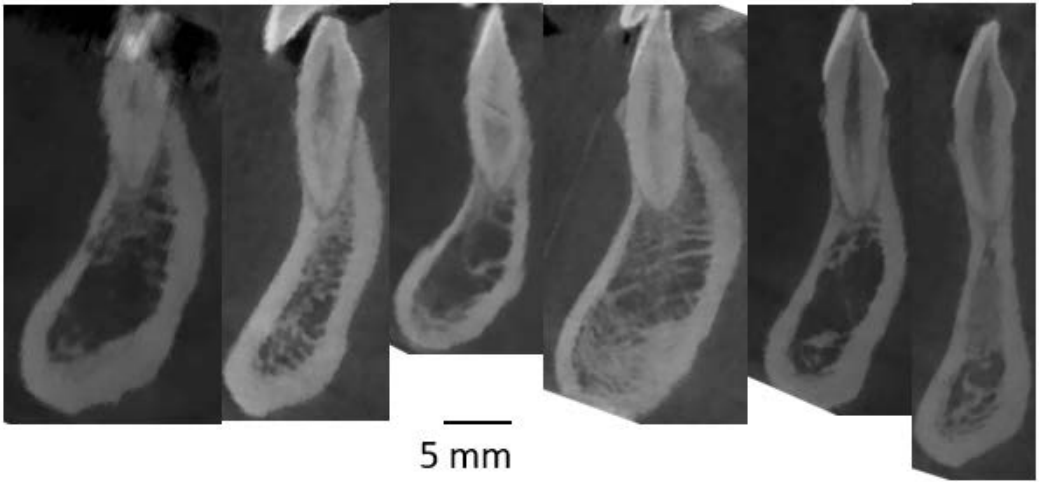
5 mm

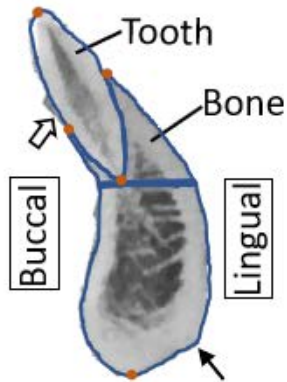
Tooth
Bone
Buccal
Lingual

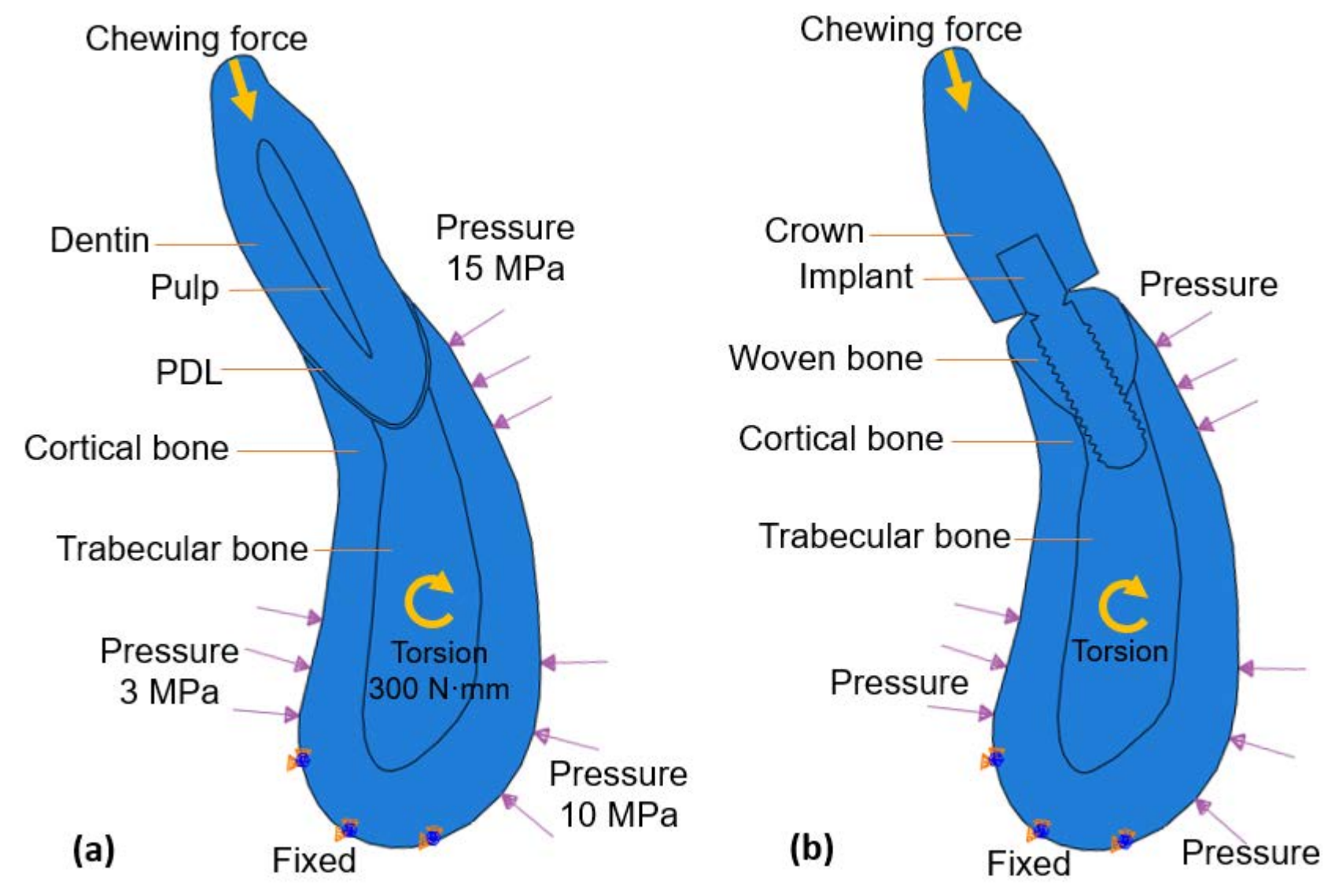
Chewing force
Dentin
Pulp
PDL
Cortical bone
Trabecular bone
Pressure
15 MPa
Pressure
3 MPa
Torsion
300 N·mm
Pressure
10 MPa
Fixed
(a)
Chewing force
Crown
Implant
Woven bone
Cortical bone
Trabecular bone
Pressure
Pressure
Torsion
Fixed
Pressure
(b)

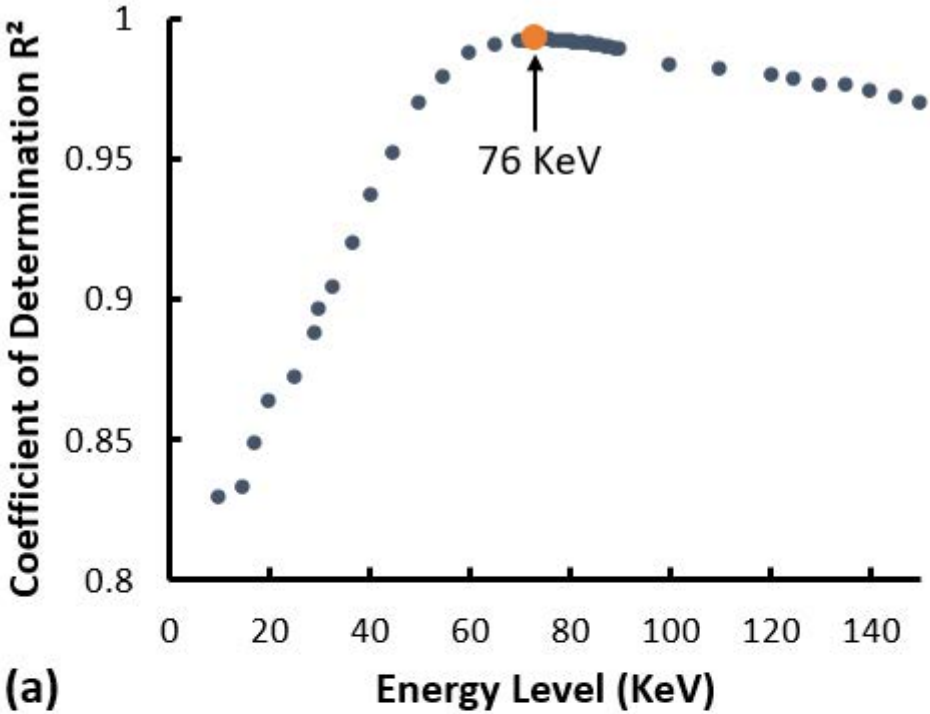
Coefficient of Determination R²
1
0.95
0.9
0.85
0.8
76 KeV
0
20
40
60
80
100
120
140
Energy Level (KeV)

(a)

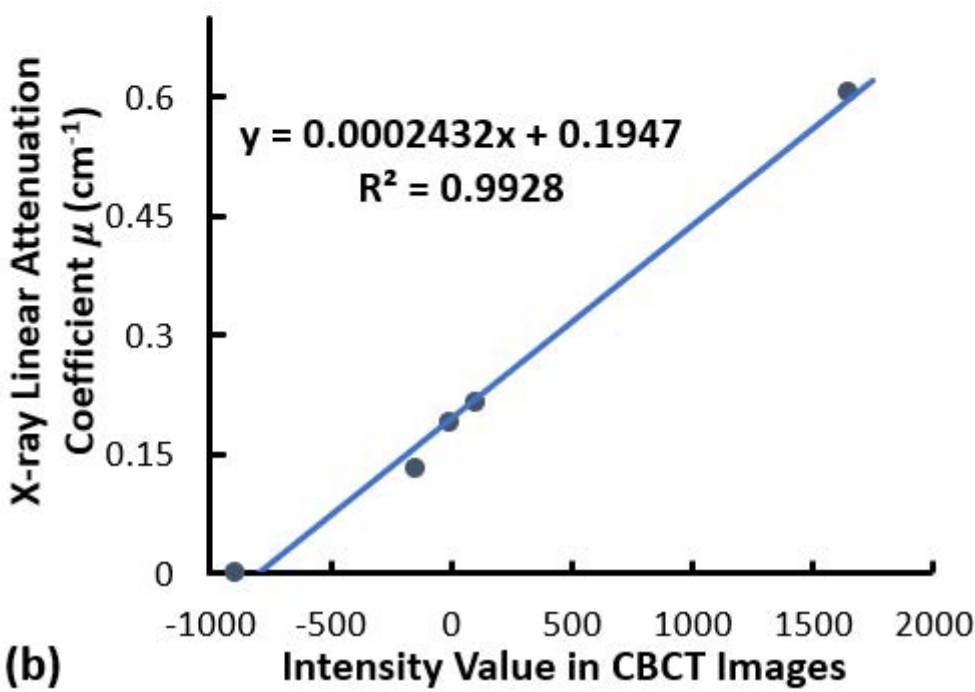
X-ray Linear Attenuation Coefficient μ (cm⁻¹)
y = 0.0002432x + 0.1947
R² = 0.9928
0.6
0.45
0.3
0.15
0
-1000
-500
0
500
1000
1500
2000
Intensity Value in CBCT Images

(b)

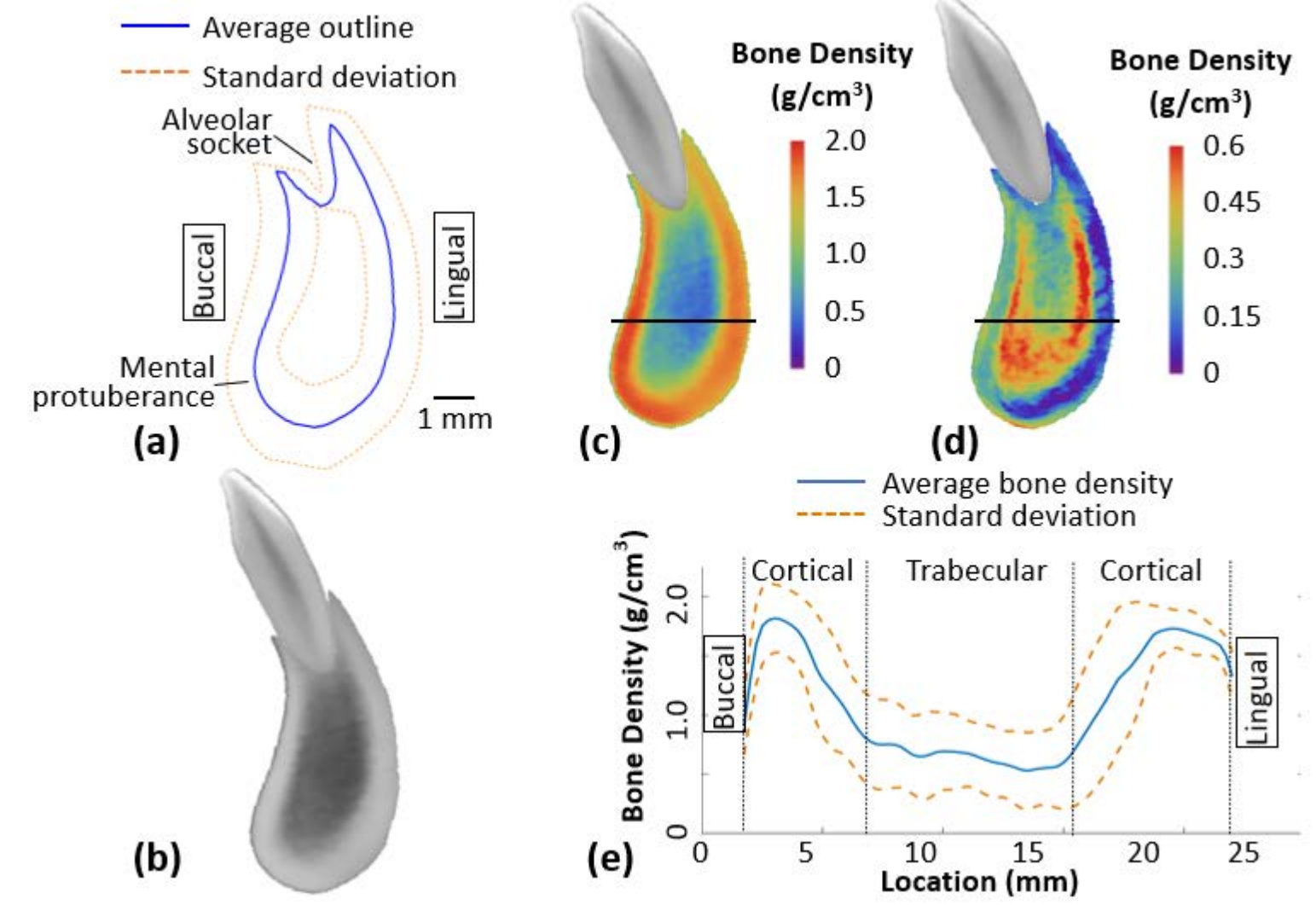
Average outline
Standard deviation
Alveolar socket
Buccal
Lingual
Mental protuberance
1 mm
(a)
(b)
Bone Density (g/cm³)
2.0
1.5
1.0
0.5
0
(c)
Bone Density (g/cm³)
0.6
0.45
0.3
0.15
0
(d)
Average bone density
Standard deviation
Cortical
Trabecular
Cortical
Buccal
Lingual
Bone Density (g/cm³)
0
1.0
2.0
0
5
10
15
20
25
Location (mm)
(e)

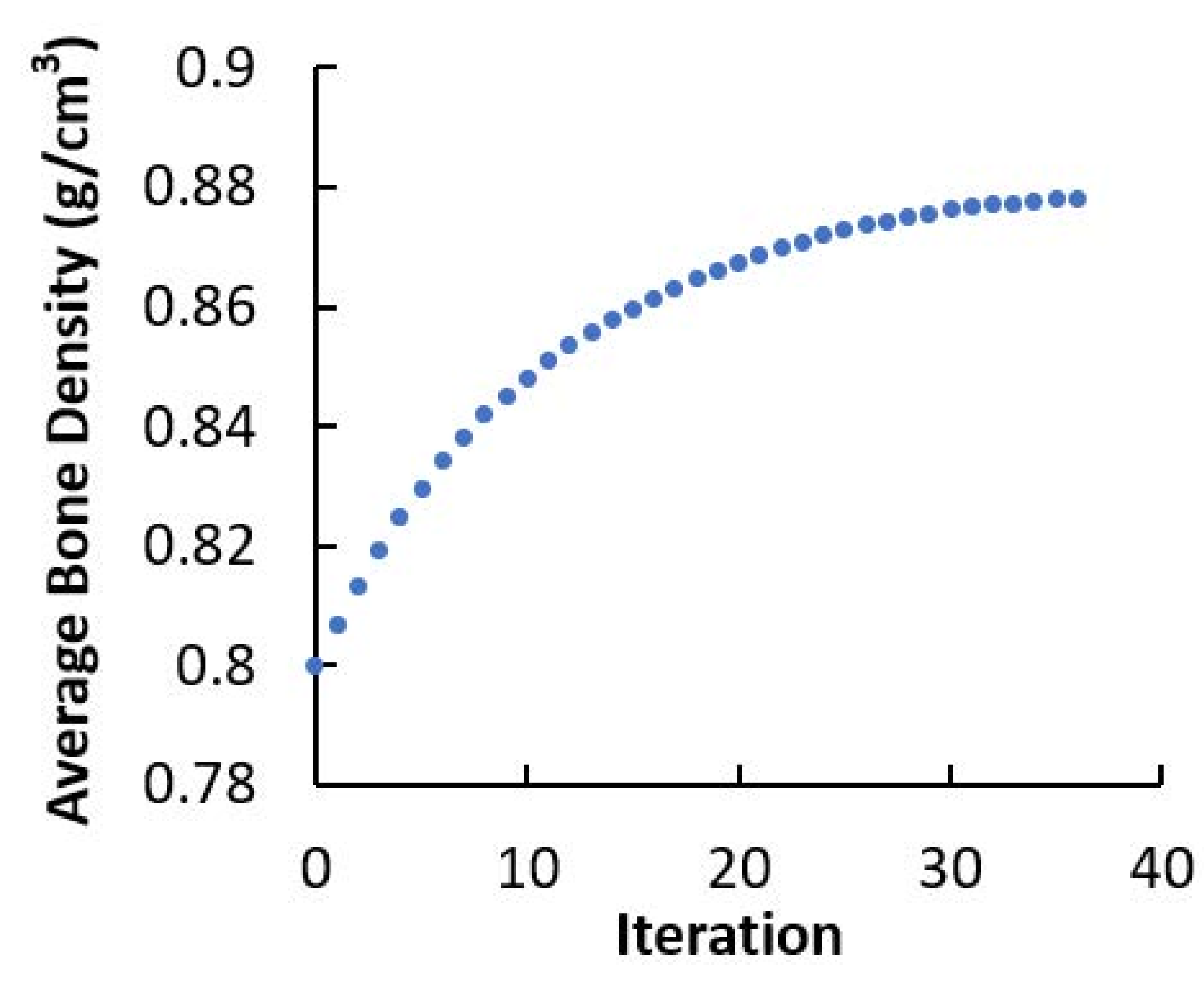
Average Bone Density (g/cm3)
0.9
0.88
0.86
0.84
0.82
0.8
0.78
0
10
20
30
40
Iteration

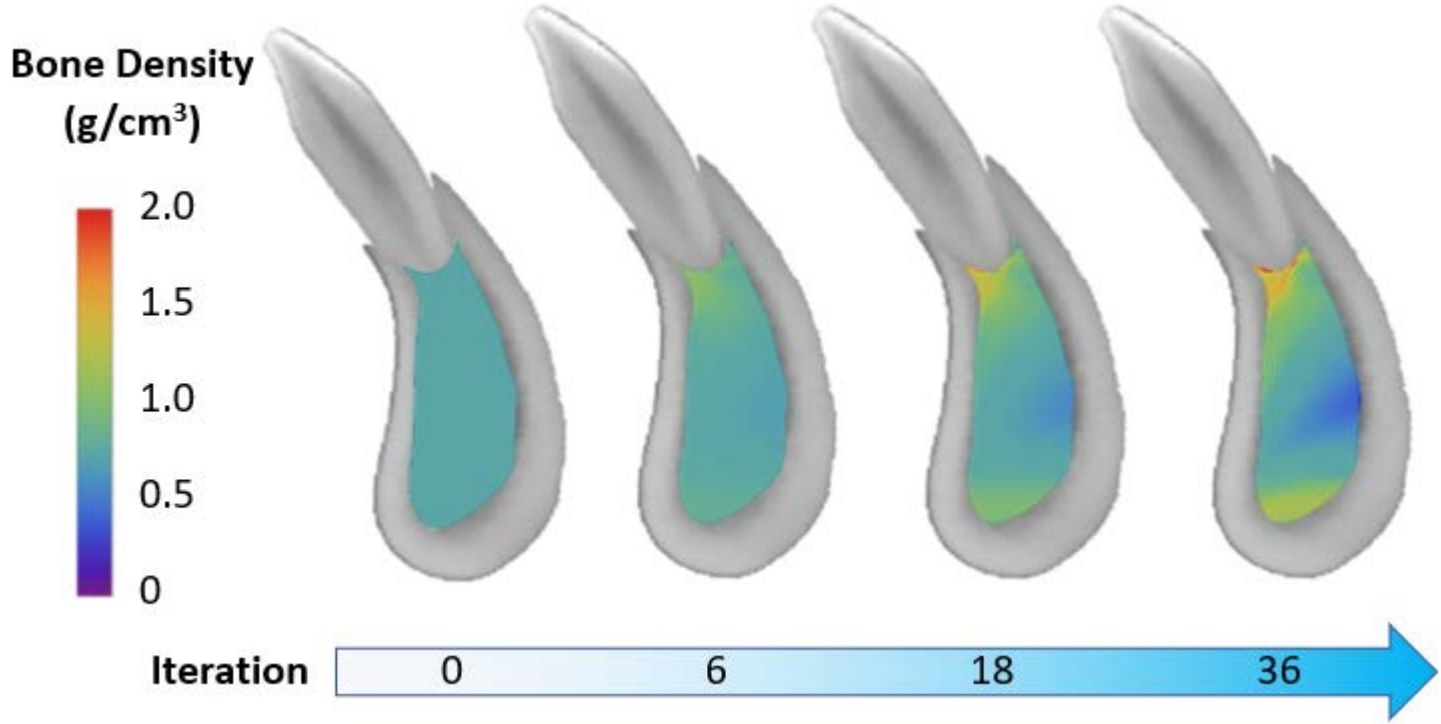
Bone Density
(g/cm3)
2.0
1.5
1.0
0.5
0
Iteration
0
6
18
36

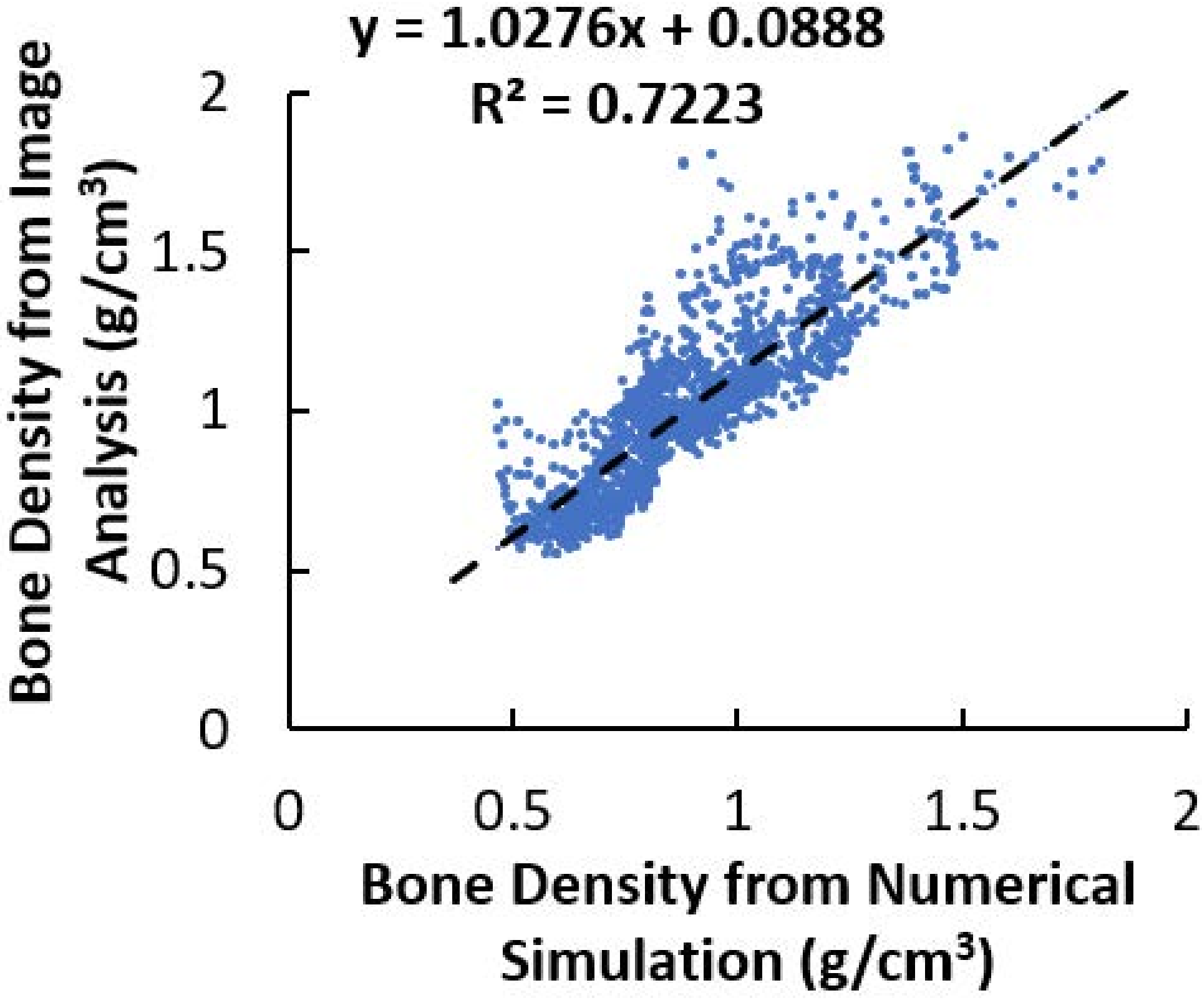
y = 1.0276x + 0.0888
R² = 0.7223
Bone Density from Image Analysis (g/cm³)
0
0.5
1
1.5
2
0
0.5
1
1.5
2
Bone Density from Numerical Simulation (g/cm³)

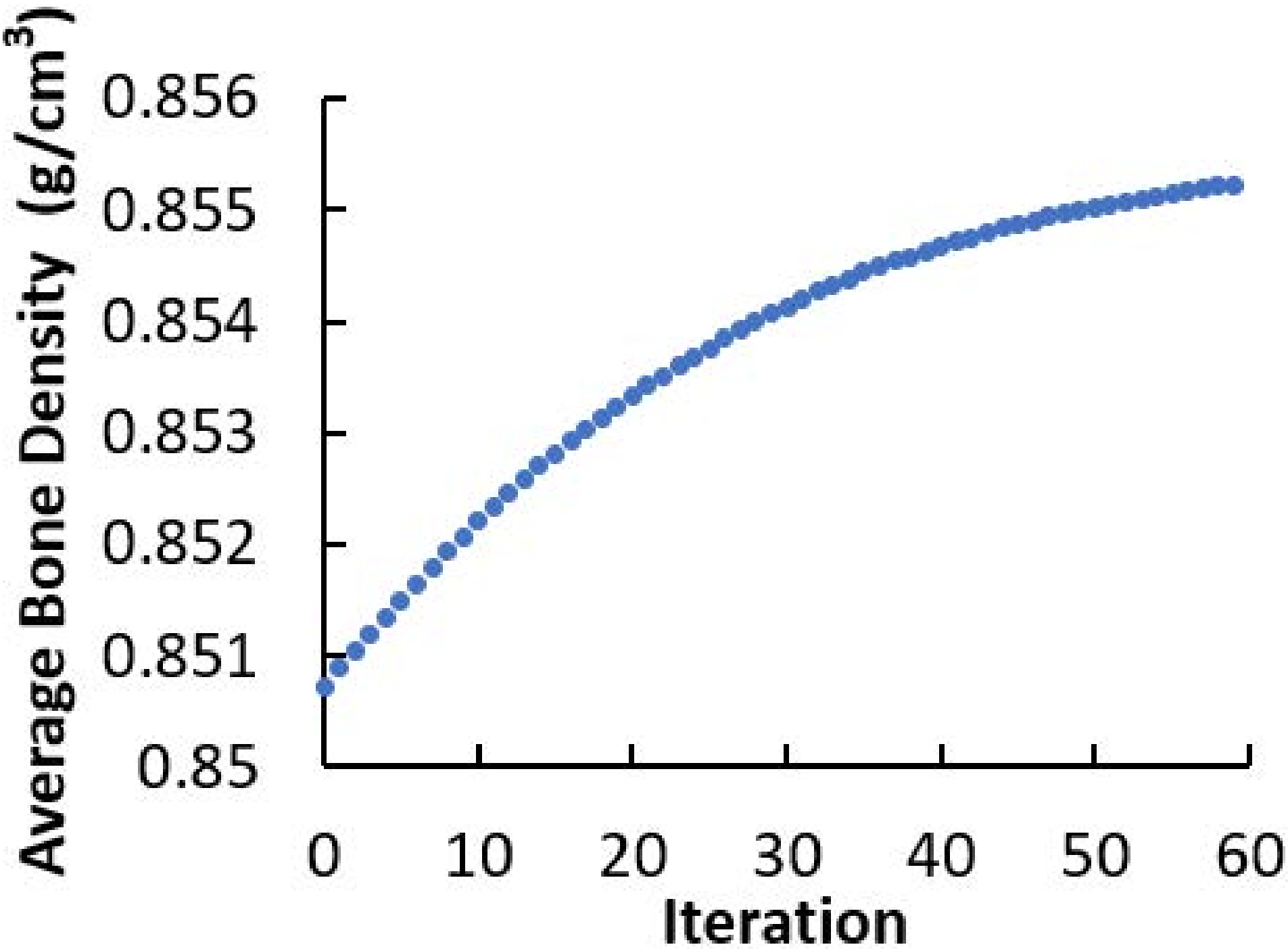
Average Bone Density (g/cm3)
0.856
0.855
0.854
0.853
0.852
0.851
0.85
0
10
20
30
40
50
60
Iteration

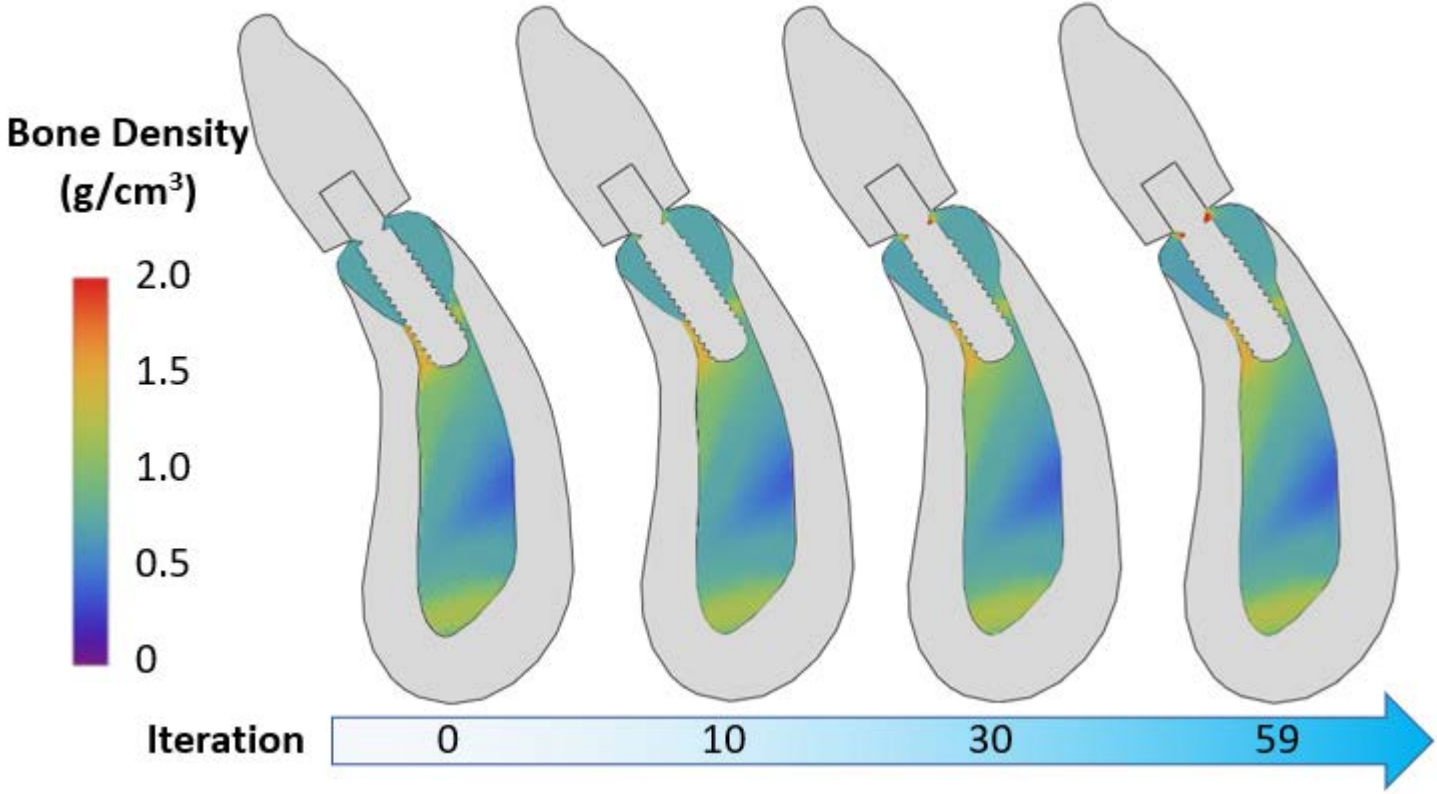
Bone Density
(g/cm³)
2.0
1.5
1.0
0.5
0
Iteration
0
10
30
59